POLITECNICO DI TORINO
Repository ISTITUZIONALE

Functional design and testing of additively manufactured milling cutting heads with enhanced structural and lubrication properties

Original
Functional design and testing of additively manufactured milling cutting heads with enhanced structural and lubrication properties / De Pasquale, G., Yudianto, A.. - In: PROGRESS IN ADDITIVE MANUFACTURING. - ISSN 2363-9512. - 10:7(2025), pp. 4165-4184. [10.1007/s40964-025-01066-9]

Availability:
This version is available at: 11583/3018046 since: 2026-11-17T15:42:56Z

Publisher:
Springer Science and Business Media Deutschland

Published
DOI:10.1007/s40964-025-01066-9

Terms of use:

This article is made available under terms and conditions as specified in the corresponding bibliographic description in the repository

Publisher copyright

(Article begins on next page)

28 November 2026

Progress in Additive Manufacturing (2025) 10:4165–4184
https://doi.org/10.1007/s40964-025-01066-9

FULL RESEARCH ARTICLE

Functional design and testing of additively manufactured milling cutting heads with enhanced structural and lubrication properties

Giorgio De Pasquale[1] · **Aan Yudianto**[1]

Received: 3 October 2024 / Accepted: 11 March 2025 / Published online: 29 March 2025
© The Author(s) 2025

Abstract
This paper describes the redesign of a face milling cutting head specifically for additive manufacturing (AM) production. The functional and structural properties were modeled and experimentally characterized for the modified version of the original component. Typically, this type of component is fabricated using subtractive processes and is characterized by its heavyweight, high torsional and compressive stiffness, and several coupled parts. Additionally, the component includes an integrated lubrication system composed of straight channels. In this study, laser powder bed fusion (L-PBF) was used to evolve the tool toward a lightweight design. The modified version consists of a single body in Ti6Al4V alloy, with a 33.9% mass reduction, lower displacements at the cutting tips, and a lower maximum stress value (− 12.2%). Furthermore, the use of parabolic-shaped channels allows the rotation of the tool to improve the lubricant flow at a uniform pressure and velocity, resulting in more refined spraying and cooling performances. The redesign also takes into account the process constraints and process-related features.

Keywords Milling cutter · Lightweight design · Additive manufacturing · Experimental mechanics · FEM · L-PBF

1 Introduction

Additive manufacturing (AM) of mechanical components has demonstrated distinct advantages over traditional subtractive manufacturing, leading to increased applications in recent years. AM enables shorter lead times from design to market, flexible customization of products, standardization of the supply chain, and flexible freeform design [1–3]. In the field of load-bearing components, AM supports (re-) design, especially through topology optimization, in situations where mass reduction is a significant target.

The traditional design of cutting heads for milling aims to optimize the static and dynamic behavior of the system composed of the milling machine, cutting head, and workpiece. More recently, the technological evolution of milling processes has focused on increasing productivity and reducing energy consumption compared to the past. The process throughput and energy needs of plants are inspiring innovative solutions in designing cutting heads and electronic controls for machines [4–8]. Of course, the real challenge behind these recent requirements is preserving, and hopefully improving, the quality of tooling performance. The machine–tool–workpiece system is characterized by mutual interactions that directly determine functional parameters such as accuracy, vibration amplitude, natural frequencies, cutting speed, and power consumption. The design requirements associated with tooling accuracy and dynamic vibrations were usually managed with the stiffness and inertia properties of the cutting head, which are both proportional to mass. High mass provides high static strength and dynamic inertia. However, heavy cutting heads also lead to drawbacks, such as reduced milling velocity, increased energy consumption for accelerating/decelerating the tool, and difficulty handling manual/automatic tools during machine setup. These limitations are in contrast with the goals of advanced milling processes. As a result, companies and research centers are developing the first attempts at advanced and modified versions of cutting heads with low mass.

Cutting head tools for milling are complex components that differ from general mass optimization problems. They are characterized by sharp dimensional tolerances, a

✉ Giorgio De Pasquale
giorgio.depasquale@polito.it

Aan Yudianto
aan.yudianto@uny.ac.id

[1] Smart Structures and Systems Lab, Politecnico di Torino, Corso Duca Degli Abruzzi 24, 10129 Turin, Italy

calibrated center of mass, high and variable angular velocities during axial rotation, and cyclic loading. Moreover, functional parts, such as the lubrication system composed of several channels and reservoir chambers, are normally present inside the head's volume. The complexity of the cutting head arises from the coexistence of geometries related to structure and function: the former is responsible for torsional stiffness, stress, displacements, and mass, while the latter provides appropriate functions for lubrication, cooling, alignment, and stability of diamond inserts, among others.

Designing such complex parts using iterative topology optimization algorithms based on FEM (finite element method) [9–13]is impractical and sometimes ineffective. Although the objective function may be identified easily (e.g., mass minimization), defining and formalizing the design variables into rigid rules for automatic iteration is extremely complicated. For instance, the optimized shape of lubrication channels requires separate structural-fluidic models that are not included in the topology optimization algorithm. However, channels and chambers contribute to the nominal objective function, and channels distribution is also essential to define mass calibration, which is necessary to reduce self-induced vibrations during rotation. Additionally, the use of design and non-design space, which is typical in topology optimization algorithms, may hinder the merging of separate parts that have mutual interactions or combined functions in the original design. This is the case, for example, of a cover separated from the main body, hosting holding screws on one side and lubrication cavities on the opposite side.

The AM process imposes constraints that greatly impact the design and result in the formation of features directly or indirectly linked to the technology. Design features directly related to the process, such as temporary supports and angles of self-supporting surfaces, are necessary for fabrication. Indirectly related design features, such as holes for powder extraction and oversized layers for mechanical tooling, are used to achieve the final shape of the component.

In conclusion, when redesigning components with high coupled geometrical and functional complexity, automatic optimization algorithms become less useful than in general mass optimization problems. Formalizing redesign methods for AM production is an ongoing effort in the community, with some references already provided [14–16]. The cutting body developed in [17] achieved an 80% mass reduction through modified design and low-density materials, resulting in at least a 50% claimed improvement in productivity. The face milling head described in [18] features an inner lattice structure to reduce global mass and distribute loads efficiently inside the component. This design solution includes an external bulk skin and 3D cellular material inside the cutting head. The lattice is also suitable for filling with viscous polymers [19–22] to absorb vibrations. In [23], this strategy was used to reduce oscillation amplitudes without a significant variation of natural frequencies, despite a slight mass increment. The reduced mass has the potential to preserve the component from time-related damage and increase its lifetime. In [24], the authors claim that the lower stiffness of the cutter increases durability and reliability. In [25–30], problems associated to design optimization of lattice components in various applications are reported.

This paper presents the evolution of the traditional shape of a milling cutting head toward a lightweight version for AM production. The redesign is supported by FEM simulations and is driven by functional and topological criteria such as mass reduction, lubrication system efficiency, optimization of structural properties (stress, displacements at cutting tips, torsional stiffness), and production rules. Functional fluidic channels have already been fabricated inside components using AM [31]. In the proposed design, the cutting head's lubrication system has a unique configuration that provides more uniform output pressure and velocity compared to the original version. This capability is achieved by parabolic-shaped channels that use the centrifugal force of the rotating head to extract the fluid. The structural analysis was performed based on finite elements method (FEM) and the fluidic simulation was conducted with computational fluid dynamics (CFD), which is based on finite volume method (FVM). The Ti6Al4V alloy (Titanium grade 5) [32–34] is used to build the component with the L-PBF (laser powder bed fusion) process. The prototype achieved a 33.9% reduction in mass and a 12.2% reduction in maximum equivalent stress compared to the original version. Although the torsional stiffness is reduced, the displacements at cutting tips are lower, which is expected to increase tooling accuracy. In the redesign, the separate parts of the original head are merged together. The modified cutting head is experimentally characterized by measuring the strain under applied torque to validate the structural properties. The comparison with model predictions shows good agreement, with a maximum deviation of 6%.

2 Design and motivations

The redesign approach utilized in this study is based on the optimization method for AM proposed by Emmelmann et al. [35]. The method involves two primary steps, namely the concept and design phases, as illustrated in Fig. 1. To accommodate the functional design features and the corresponding functional variables, an additional step for functional optimization has been incorporated into the original flowchart. Given the parallel calculations involved, i.e. multi-physical simulations, it is impractical to integrate all the design variables into a single optimization process.

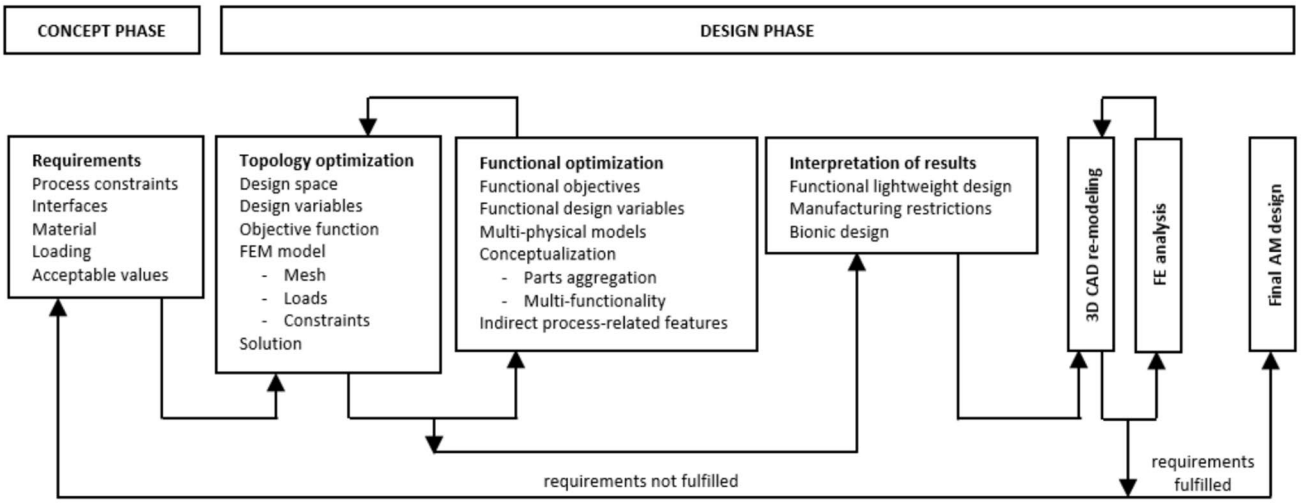

Fig. 1 Design for AM process according to [35] with integration of the functional optimization step

2.1 Original component description

The cutting head under consideration has a diameter of 125 mm, a height of 58 mm, and is fitted with eight inserts to hold eight polycrystalline diamond (PCD) cutters. The original version of the head comprises two separate parts, namely the main body and the cover, which are joined by an ISO M20 screw aligned with the rotation axis. The eight inserts are positioned at 45° angular intervals around the perimeter and house eight cutters, each held in place by conic holders coupled by ISO M8 and M5 screws. The total mass of the cutting head is 1941.3 g. Figure 2a shows a photograph of the original cutting head tool, while Fig. 3 depicts a drawing of the same tool. With reference to a milling machine with average performance (36 kW), the following working conditions are considered as reference: 10,000 rpm maximum rotational velocity (3926 m/min maximum cutting speed), 0.2 mm maximum shaving thickness (0.127 mm on average), 2394 mm^2 maximum shaving area, 1600 N maximum cutting force on single cutter (1104 N on average), 555 N average force per revolution on single cutter, and 34.69 Nm average torque per revolution on single cutter. The cutting head material is Titanium Grade 5 (Ti6Al4V) with a Young's modulus of 104 GPa, a Poisson's ratio of 0.31, a shear modulus of 41 GPa, a density of 4428 kg/mm^3, a yield stress of 827 MPa, and an ultimate stress of 1050 MPa.

The lubrication system comprises eight radial channels directed toward the perimeter cutters and four axial channels directed to the top surface, as illustrated in Fig. 3. The former channels lower the cutters' temperature through the lubricant spray produced at the output, while the latter provides debris removal. All channels originate from a ring-shaped reservoir, which has a flat shape and is positioned inside the head. It serves as a fluidic capacitance that reduces the variability of lubricant flow under different operative conditions. The machine's primary lubrication supply channel, located inside the milling shaft, feeds the reservoir via four 5 mm-diameter channels.



Fig. 2 Cutting head tool: original version (**a**), redesigned lightered version for AM (**b**), and cross section view of redesigned version (**c**)

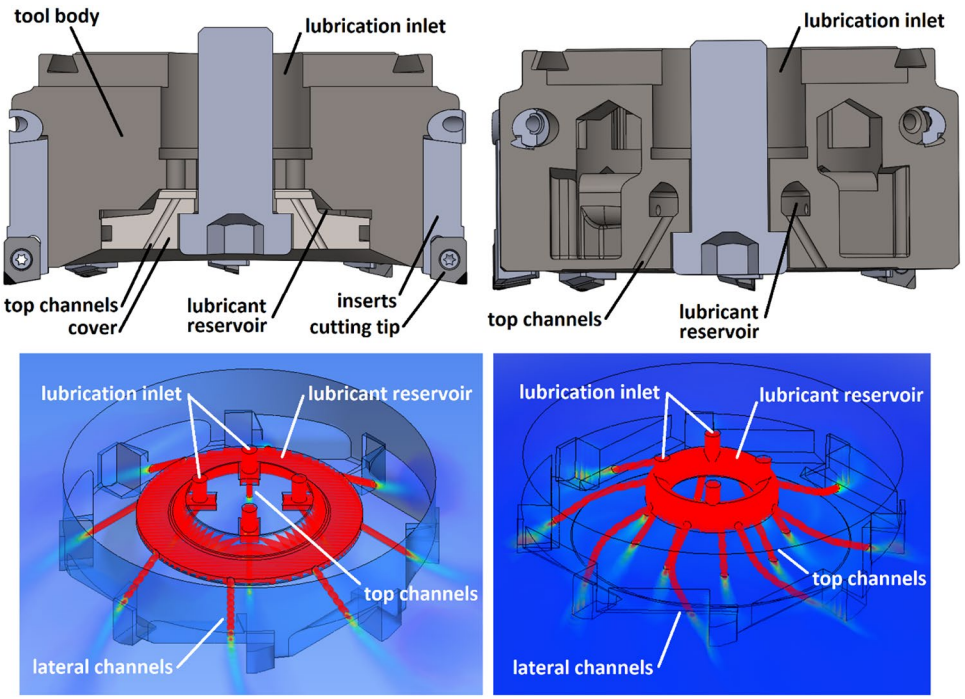

Fig. 3 Comparison of cutting head tool component and lubrication system in the original (left) and modified (right) configurations

2.2 Redesigned component description

The redesign of the cutting head is based on the eight intermediate steps presented in Fig. 4. The details of each design step include the constraints related to the AM process, such as temporary supports, part orientation, volumes oversizing for tooling, and powder management and extraction. The original component (1) is redesigned to integrate the cover and various smaller components into a single part (2). The internal volume is modified to reduce mass by incorporating a circular cavity (3), and straight lubrication channels directed toward the front surface are

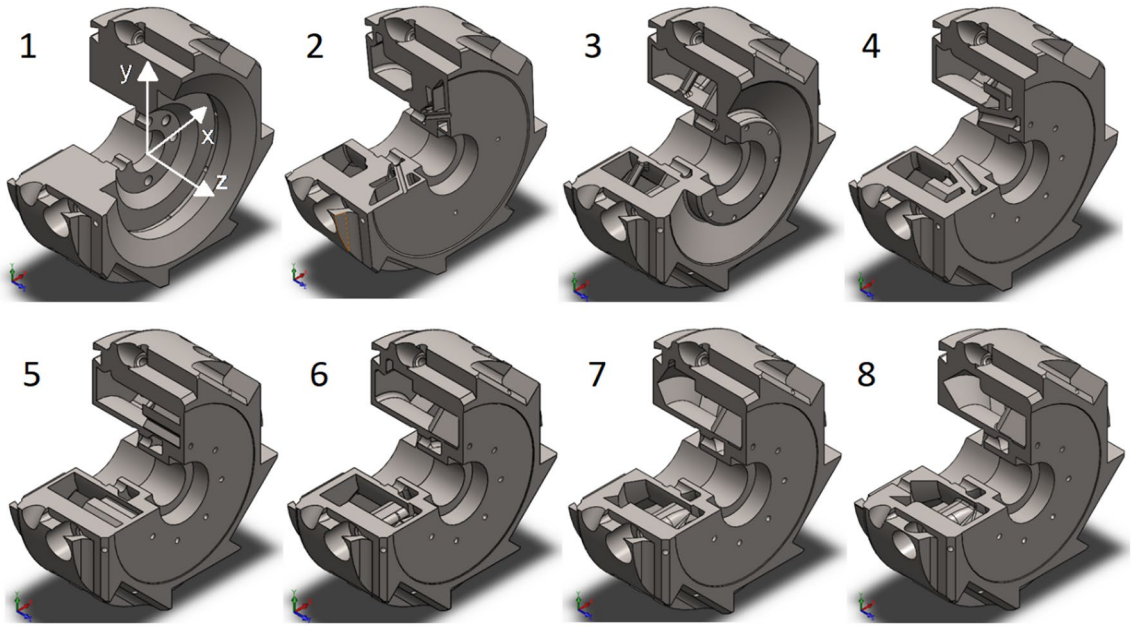

Fig. 4 Evolution of the component topology from the original component (1) to the final shape (8), based on successive steps of redesign. Each design step accounts for progressive topological weight/strength ratio optimization, functional optimization, and process constraints

added (4). Additionally, parabolic channels for lubricating the cutting elements and further optimization of the internal reservoir are implemented (5, 6). The roofs of the internal cavities are oriented at appropriate angles to ensure self-supporting during the manufacturing process (7) and extraction holes for powder removal introduced (8). The optimization process includes, as target functions, mass reduction and global stiffness maximization; however, additional functional targets are considered such as the fluid flow optimization and inner fluid chamber creation. The constraints of the optimization are the external volume and shape that are preserved almost unchanged. Additional information regarding the process-related design constraints is provided in Sect. 4. The topological optimization method is applied, where the objective function is to minimize the overall mass. As mentioned earlier, the iteration algorithms implemented in multipurpose software are inadequate for optimizing the coupled topological and functional properties. In fact, the component's functional and shape complexities necessitate the direct involvement of the designer to define all the details involving knowledge of production processes and tool utilization.

The details considered in the design process encompass various factors, such as admissible wall thickness at different points, extra material required around threaded holes, channel shape and distribution, self-supporting ability of inner surfaces, and more. As such, every intermediate variation is designed by computing the stress distribution within the component and then modifying the part by removing the least loaded material to ensure that the stress does not exceed the yield threshold at each step. Strain distribution and displacement configuration are also calculated to meet the functional requirements. Furthermore, direct evaluation by the designer ensures that all functional requirements are met at every intermediate step, which would otherwise be overlooked. The final version accepts a 25% reduction in torsional stiffness in accordance with commercially available milling tools' properties [36].

Following the redesign, the component volume is reduced by 33.9%, from 438,413 mm^3 (404,941 mm^3 for the main body and 33,472 mm^3 for the cover) to 289,598 mm^3. The mass reduction percentage is also 33.9%, from 1941.3 g (1793.1 g for the main body and 148.2 g for the cover) to 1282.3 g. In the modified component, the moments of inertia calculated with respect to the center of mass decrease by approximately 83% along all three axes. The merger of the body and cover eliminates the possibility of lubricant leakage through the coupled surfaces. The redesign primarily focuses on the cutting head's inner part, while the outer shape remains mostly unchanged. This is due to the need to preserve the mechanical coupling surfaces with the milling machine and inserts and maintain the cutters' relative distances.

The AM process allows the creation of internal cavities and channels during component fabrication. For this reason, the main body and cover of the cutting tool are merged to create a single part, as shown in Fig. 2b and Fig. 3. The cavities created inside the head include the lubricant reservoir, channels, and some free volumes that are used for mass reduction. The configuration of the channels in the redesigned tool is shown in Fig. 3. The new lubricant reservoir results from the merging of the body and the cover, with its volume increasing by 10.4% (from 5717 to 6311 mm^3), and its shape becoming more rounded compared to the original version. This new shape increases the fluid inertia inside the reservoir and improves the attenuation of flow variations. The number of axial channels is increased from four to eight to improve the ability to remove chips from the workpiece. The axis of lateral channels, originally straight, is changed to parabolic to increase the output velocity of the lubricant by exploiting the centrifugal force. The modified lubrication system provides more uniform flow and pressure, and increased output radial velocity of the lubricant, according to the simulations reported in Sect. 3.

2.3 Cost analysis

A quantitative evaluation of the cost factors affecting additive manufacturing (AM) and traditional manufacturing (TM) is necessary to define the operational feasibility of AM in industrial applications. The cost structure of an AM-produced milling cutting head is influenced by various parameters, including build time, material efficiency, post-processing operations, and component lifespan. This analysis provides a comparative assessment based on process-specific data and existing literature, aiming to highlight the current limitations and potential advantages of AM.

Production costs. The production cost of AM components is primarily driven by machine operating time, which is a function of part volume, laser power, layer thickness, and scan strategy. For the specific case analyzed, considering a four-laser L-PBF system with a build rate of approximately 20 cm^3/h and an estimated bulk density of 4.43 g/cm^3 for Ti6Al4V powder, the total build time for a single cutting head (289.6 cm^3) is approximately 14.5 h. Assuming a machine operating cost of 60–80 €/h, the estimated direct manufacturing cost per part is in the range of 870–1160 €, excluding powder, support removal, and heat treatment.

Conversely, TM involves milling operations from a Ti6Al4V billet, with material costs typically ranging from 50 to 70 €/kg. Given the initial billet weight of ~ 2.8 kg and a final part mass of 1.28 kg, material waste is estimated at 54%, leading to a raw material cost of 140–200 €. Subtractive manufacturing, despite higher material usage, benefits

from significantly lower processing costs, with roughing and finishing operations requiring approximately 4.5 h at a machine rate of 40–50 €/h, resulting in a cost range of 180–225 €. Thus, the direct manufacturing cost for TM is estimated at 320–425 €, indicating that AM fabrication is currently 2.5 to 3.5 times more expensive.

Post-processing, material utilization and tool-life performance. Post-processing for AM includes support removal, stress-relief heat treatment, and finishing. Wire-cut EDM or CNC milling is required to remove supports, adding 50–80 € per part. Heat treatment at 650–800 °C for residual stress relief adds 30–50 €. The final machining of critical surfaces (e.g., tool interface and cutting insert seats) requires 1.5–2 h of CNC milling, contributing an additional 60–100 €. In contrast, TM requires only final precision machining, estimated at 60–80 €.

Material utilization is a crucial factor in cost efficiency. AM powder reuse has been studied extensively, with reports indicating that up to 95% of unfused powder can be recycled without significant degradation in mechanical properties [37]. Thus, AM exhibits a material utilization efficiency of ~ 85%, while TM produces significant non-recoverable waste, impacting sustainability.

From an operational standpoint, AM cutting heads offer benefits in weight reduction (− 33.9%), optimized lubrication channels, and improved insert cooling. The reduced thermal loads on cutting edges are expected to extend tool life by at least 50–100%, translating into fewer tool replacements and potential cost savings. However, these advantages must be balanced against the higher initial acquisition cost and the current build rate limitations of AM machines, which may constrain scalability.

Industrial viability and challenges. While AM production of milling cutting heads remains economically challenging in single-part production, it becomes more viable in batch manufacturing scenarios, where machine utilization efficiency is maximized. Studies suggest that AM cost-per-part can be reduced by 15–30% when printing multiple components per job [38]. Nevertheless, challenges such as limited build size, residual stress management, and surface finish quality must be addressed to fully unlock AM's industrial potential.

Based on these considerations, AM is not yet universally competitive with TM in terms of cost, but it presents opportunities in lightweight, high-performance tooling applications, particularly where extended tool life and optimized functionality offset the initial cost differential. Future advancements in process speed, automation, and material economics will be key in determining the long-term industrial adoption of AM for milling tool production.

3 FEM simulations

The properties of the cutting head tool are determined using FEM models in both the structural and fluidic domains. In the former case, the distribution of stress and strain is calculated under steady-state conditions that correspond to the heaviest loading. This includes cutting forces, pre-load on screws, and centrifugal force. In the latter case, the lubricant pressure and velocity distributions are calculated as functions of rotational velocity. Both models are utilized for the design optimization of the component described previously, as well as for the modifications of the lubrication system.

3.1 Structural models

A tetrahedral element mesh-based discretization is employed, with element sizes imposed within the range of 0.5–3 mm. Identical mesh criteria are utilized for all simulations. The 3D geometrical modeling is conducted using SolidWorks, and numerical simulations are performed using HyperWorks software, respectively. Element distortions and mesh size-related convergence are verified. The mesh of the structural model is illustrated in Fig. 5a.

The model comprises three types of loads: cutting torque, compression provided by screws, and centrifugal force due to rotation. The loads system of the first refers to the

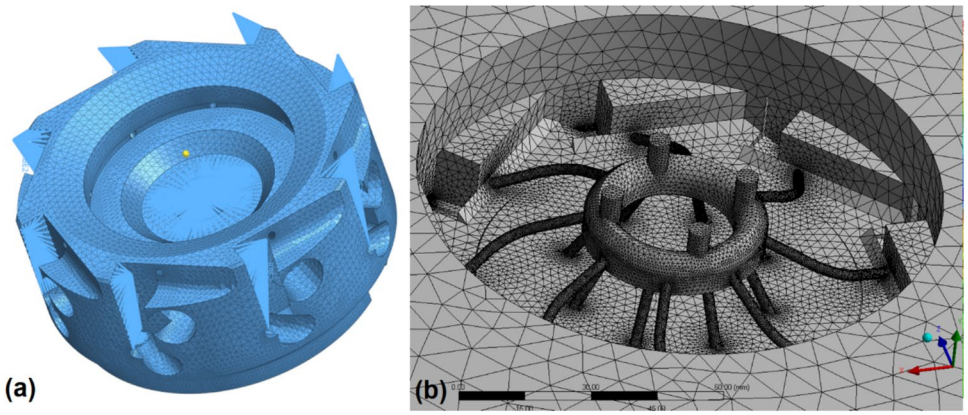

Fig. 5 FEM model of the cutting head tool for structural simulations (**a**) and CFD simulations of the lubrication system (**b**)

theoretical worst-case operational condition, represented by eight cutting forces at the maximum value of 1600 N. In actual conditions, only four cutters may exchange forces with the workpiece simultaneously, while the other ones are in discharge mode. Hence, the real case corresponds to an average force of 555 N per revolution on each cutter. However, the overestimation of the load provides the safety factor required to account for the intensification effects caused by vibrations, which are neglected in the static simulation. On the one hand, eight cutting forces at maximum value represent the worst-case operative condition, while the real force system composed of only four cutting forces results in asymmetrical loading of the tool, which is less critical. For simplicity, the inserts and cutting tips are considered as rigid bodies and are not included in the FEM model. Therefore, the actual application point of the cutting forces is located outside the volume, and the forces application points are connected to the structure through rigid virtual links.

The second load system applied to the structure is generated by the screws holding the cutting head to the milling machine and those holding the inserts to the lateral surface. The force generated by each screw is a compressive preload aligned to its axis. The main central screw (ISO M20) is tightened at 290 Nm prescribed torque, corresponding to 68.41 kN axial force applied through the central body and the cover. The inserts are held by eight ISO M8 and eight ISO M5 screws, tightened at 13 and 4 Nm torques, respectively, corresponding to 9.85 and 4.85 kN. The axial forces generated by the screws are modeled by rigid virtual links connected to the structure surfaces.

Finally, the third load system consisting of the centrifugal force caused by rotation is applied to each node of the model. The nodal forces are computed as a function of the tool's angular velocity, the material density, and the radial distance from the rotation axis.

The displacement constraints are applied to the surface connecting the milling machine and the tool to reproduce the real configuration. The translation in the vertical direction (z-axis in Fig. 4) is imposed to zero, and the axial rotation is constrained at the surfaces of clamping with the machine shaft.

3.2 Fluidic models

The fluidic model is generated by considering the volumes of the channels, inner reservoir, and the environment volume surrounding the cutting head tool. The 3D geometry of the fluidic model is created using SolidWorks software, and the numerical CFD model is generated by Ansys CFX, which is based on the finite volume method. The lubricant inlet is located at the connection between the tool and the milling machine shaft, and the fluid inlet is provided by four channels with a 5 mm diameter. The surrounding volume of air included in the model, with dimensions of $350 \times 350 \times 170$ mm^3, has the lateral surfaces constrained at atmospheric pressure. The flow through all the lateral surfaces is permitted, except for the rigid wall simulating the workpiece, which is defined as a no-slip wall with a smooth surface.

The fluids defined in the model are the lubricant and air. The lubricant is a mixture of 85% water and 15% cutting fluid, which is typically identified as alkaline electrolyzed water. The density of cutting fluids ranges from 0.95 to 1.05 g/cm^3 [39], and in the simulations, the lubricant mixture is modeled as a fluid with a density of 0.997 g/cm^3. The air properties are defined at a temperature of 25 °C with a continuous fluid morphology. The standard k-epsilon model is used to describe the turbulent flow in the CFD calculation. This model offers the simplest level of enclosure, as it has no dependence on the geometry of the flow regime input [40].

The tetrahedral-shaped fluidic elements, with sizes ranging from 0.25 to 51 mm and 1.20 growth rate, are used in the model to account for the smallest features in the channels and the extended surrounding air volume. The mesh definition is validated through sensitivity analysis, and Fig. 5b reports the lubrication channels and air volume CFD model in the final redesigned version of the cutting head.

The lubricant velocity imposed at the channels inlet is calculated from the properties of the lubrication pump installed on the milling machine, corresponding to a range of 77.6–126.7 m/s. The maximum angular velocity of 1047 rad/s (or 10,000 rpm) is imposed on the model, with a pressure boundary condition defined at 1 atm or 101,325 Pa at the lateral surfaces of the air volume. The described model is solved by transient analysis with a total time of 0.5 s and a time step of 0.001 s. To ensure the accuracy of the fluidic simulation with the applied mesh, the maximum Courant–Friedrichs–Lewy (or CFL) number was ensured to be ~ 1, which resulted from the fixed time step of 0.001 s.

4 Fabrication by AM

The redesigned component is fabricated using the laser powder bed fusion (L-PBF) additive manufacturing process with Ti6Al4V alloy. During fabrication, the alloy powder is exposed to a laser beam, which enables the layer-by-layer growth of the component [32, 33]. The production process is carried out using the Renishaw AM 500Q system. Given the complexity of the component's shape, careful consideration is required for both its orientation and support strategy. The optimal orientation was determined with the flat side of the cutting head parallel to the machine's build platform, as this provides uniform accuracy along the lateral surface, which grows perpendicularly (at 90°) to the platform in every area. The component orientation and support strategy are represented in Fig. 6. Vertical supports, each 5 mm in

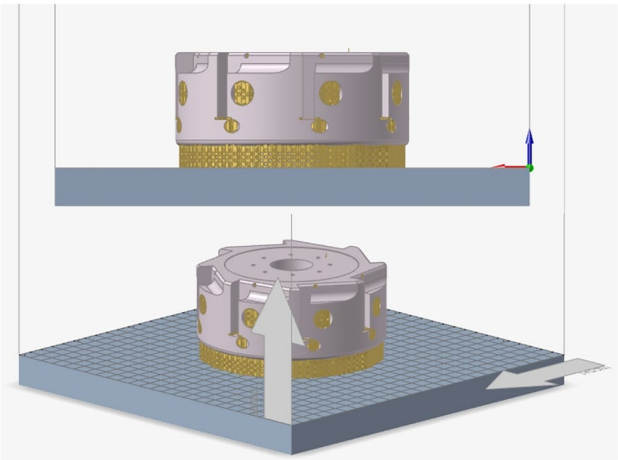

Fig. 6 Component orientation and support strategy (supports volume $3.139 \cdot 10^6$ mm^3, supports area $1.048 \cdot 10^5$ mm^2, printing time 40.44 h)

length, are uniformly distributed beneath the flat side of the component. These temporary supports offer thermal insulation from the platform and facilitate the physical separation necessary for part removal via a wire cutter. All surfaces with angles between 0° and 45° require support. To this end, support structures are defined using software, determining both their positioning and dimensions. The internal vacuum regions of the component are deliberately left unsupported for two reasons: first, post-fabrication support removal is not feasible, and additional supports would increase the overall mass. Second, fragile supports inside the component may break during use, leading to unwanted noise or the sensation of foreign objects. Thus, the surfaces of the internal vacuum regions are designed to be self-supporting, adhering to a minimum orientation angle of 45°. Additionally, the channels are self-supported, as their dimensions (4 mm) are below the critical threshold of 6–7 mm. For larger channels, self-supporting capability can be ensured by adopting a "drop shape" cross section, created by incorporating two 45° tilted surfaces at the top of the channel.

Another critical design requirement involves the removal of unmelted powder from the internal cavities of the component. To achieve this, all internal cavities are interconnected and linked to the external environment via two designated holes, which facilitate powder extraction. After powder removal, the holes are threaded and sealed with plugs to prevent the ingress of dust, debris, and lubricant into the tool. The L-PBF process generates components with surface roughness ranging from 5 to 40 µm [41] and dimensional accuracy within a few tenths of a millimeter [32]. Consequently, the nominal design must account for an additional material layer on all surfaces requiring post-processing to meet functional tolerances. In this case, the surfaces designated for mechanical reworking are oversized by a layer with a thickness of 1.5 mm.

5 Experimental characterization

The experimental setup described in this section aims to replicate the steady-state load applied to the tool during operation, specifically resulting from the cutting torque and the compression of the screws. The centrifugal load due to rotation is not considered in this setup. Static loads are applied to the cutting head using the uniaxial servo-hydraulic universal testing system (UTS) Instron 8801, equipped with a 100 kN load cell, and by tightening all functional screws to the specified torque. The tensile force exerted by the machine is converted into torsional torque, simulating the cutting torque, through a custom-designed clamping system. This clamping system consists of two arms positioned at a radial distance $d = 137$ mm from the cutting head axis, producing a torque $C = F \cdot d$, where F is the tensile force applied by the machine. The test setup is illustrated in Fig. 7.

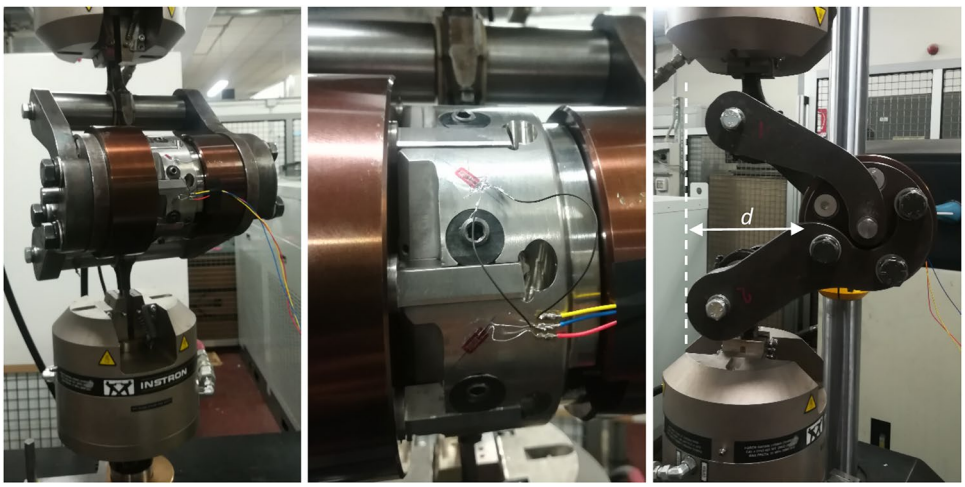

Fig. 7 Experimental setup for the static characterization of the original and redesigned cutting heads: the tool mounted on the testing machine with the clamping system (left), a close-up of the strain gauges in the half-bridge configuration (center), and a lateral view of the clamping system used for load conversion (right)

Two strain gauges with a resistance of 120 Ω, configured in a half Wheatstone bridge setup [42], were applied to the lateral surface of the cutting head. The output from the strain gauges was recorded using the HBM QuantumX MX1615B amplifier and analog-to-digital converter, and processed with the HBM Catman software. In accordance with the simplified torsional bar model, the sensors were oriented at a 45° angle relative to the axial direction. Unlike the theoretical cylindrical model, additional strain gradients induced by local geometrical features were present and included in the measurement. Nonetheless, the actual strain values were compared with the calculations provided by numerical simulations on the real geometry. An axial load ramp from 0 to 5 kN (corresponding to a torque of 685 Nm) was applied and subsequently released.

The performance of the cutting head tool was evaluated during machining operations, taking into account the interaction between the tool, the milling machine, and the workpiece material. Particular attention was given to the modified lubrication system, which was compared to the original design in terms of debris removal efficiency and cooling performance. The representative image in Fig. 8 illustrates the directionality and intensity of the lubrication flow, highlighting the differences between the original and the optimized components.

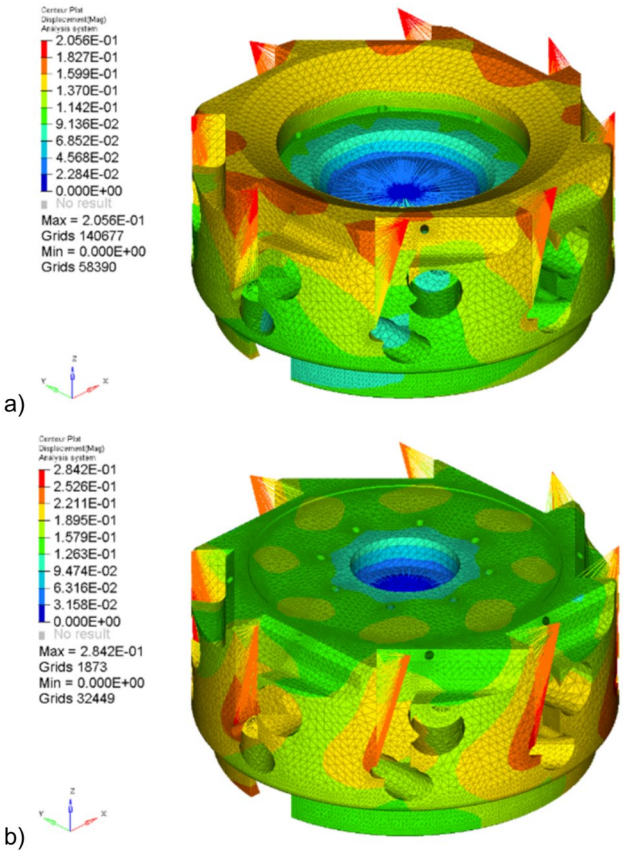

Fig. 9 Total displacements (mm) from FEM structural simulations under the combined effects of cutting torque, screw compression, and centrifugal force: original (**a**) and redesigned (**b**) components

6 Results and discussions

6.1 Results of structural modeling

The individual and combined effects of the loads applied in the FEM structural model, including cutting torque, screw compression, and centrifugal force, were computed. The operating conditions of the cutting head involve high rotational velocity and relatively low torque, making the stress induced by rotation significant. Under the loads and constraints described, the results for both the original and redesigned components are presented in Figs. 9 and 10.

The calculated stress distribution indicates values below the material's yield threshold. The maximum Von Mises equivalent stress decreases from 974 MPa in the original component to 855 MPa in the modified version. The maximum overall stress, as depicted in Fig. 10, is the vector sum of stress components caused by rotation (969 MPa in the original head and 858 MPa in the modified head) and cutting torque (184 MPa in the original head and 330 MPa in the modified head). The effect of screw compression is negligible at the nodes where maximum overall stress occurs. Comparing both cases, the stress contribution from

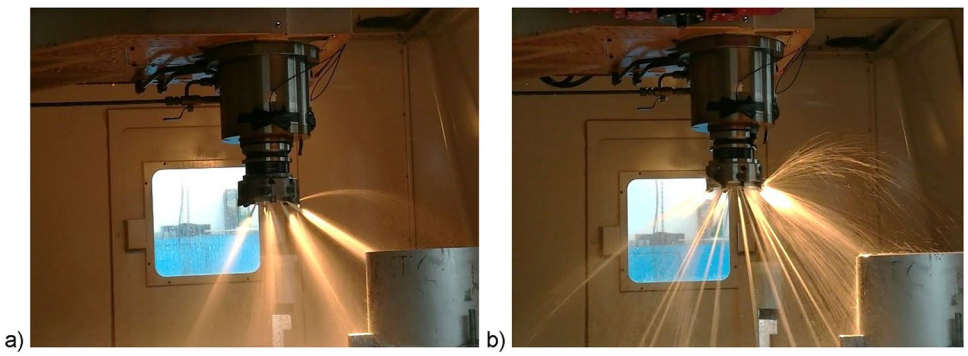

Fig. 8 Comparison between lubrication flow in the original (**a**) and optimized (**b**) components, captured during the preliminary setup operations of the milling machine

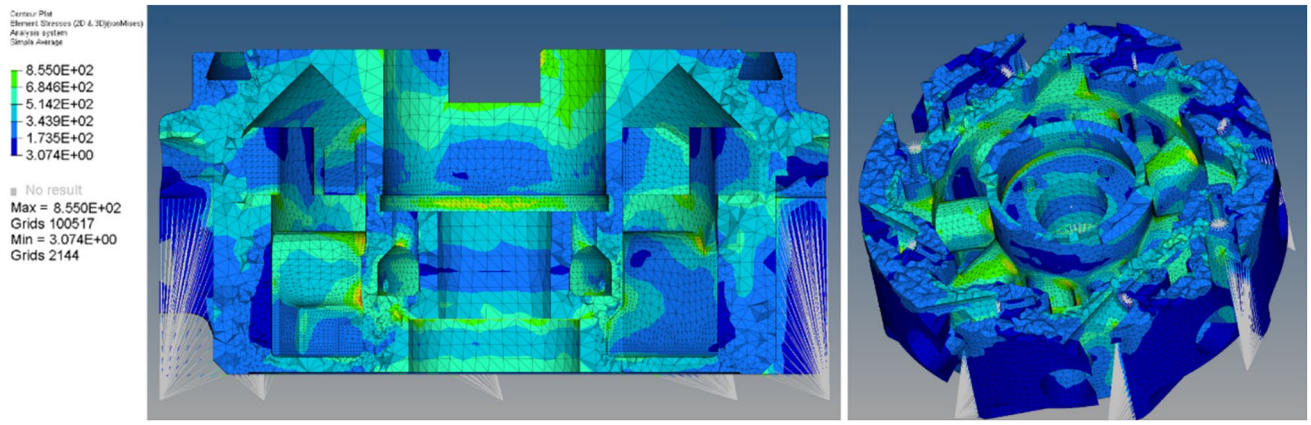

Fig. 10 Cross-sectional views of von Mises stress distribution (MPa) from the combined load effects in the redesigned component

cutting torque increases from 18.9% in the original component to 38.6% in the redesigned component.

In the original component, the maximum displacement is 0.206 mm, located at the periphery of the tool. This displacement results from the vector sum of displacements due to rotation (0.192 mm) and cutting torque (0.0261 mm). The effect of screw compression is also negligible at the nodes where the maximum displacement occurs. A similar situation is observed in the redesigned component, where the maximum displacement of 0.284 mm is composed of displacements due to rotation (0.276 mm) and cutting torque (0.0351 mm). Therefore, in both geometries, the contribution of displacement caused by rotation remains almost constant: 97.3% in the original tool and 97.1% in the redesigned tool.

The computed stress and displacement values under combined and separate loads (centrifugal force and cutting torque) are reported in Fig. 11 for the original shape, the intermediate shape (identified as step number 4 in Fig. 4), and the final shape.

The maximum stress is reduced in the redesigned version, primarily due to the integration of the cover with the main body and the modified geometry of the central hole for the M20 screw. These modifications eliminate sharp corners and other geometric features that previously contributed to local stress concentration. In the original component, the highest displacement values occur near the inserts and cutting tips, potentially leading to inaccuracies in cutting precision. In contrast, the redesigned version exhibits more uniform local displacement values around the same functional areas, despite a reduction in global stiffness resulting from the geometry optimization for weight reduction. This improvement is visible in Fig. 9, where the local displacements around the cutting tips reduces from about 0.206 mm (original component) to 0.189 mm (modified component).

The torsional stiffness is calculated as the ratio between the applied torque and the torsion angle between the two planar surfaces of the tool. An applied torque of 800 Nm is generated by the application of eight forces of 1600 N at the cutting tips. The torsional stiffness decreases from 37,118

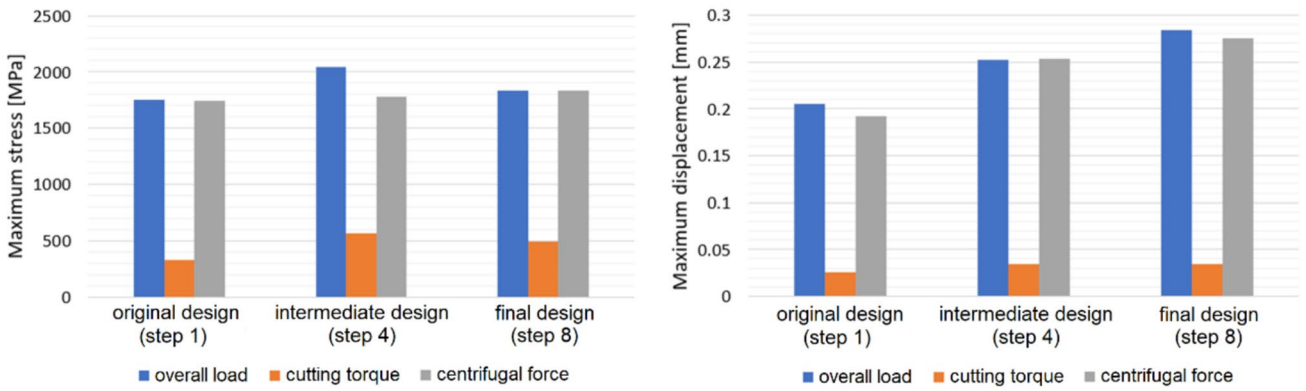

Fig. 11 Equivalent maximum stress (left) and displacement (right) calculated by FEM for three design iterations (corresponding to shapes 1, 4, and 8 in Fig. 4) under the combined load, cutting torque alone, and centrifugal force alone

Nm/deg in the original component to 27,974 Nm/deg in the redesigned component, representing a 24.6% reduction.

6.2 Results of fluidic modeling

6.2.1 Effect of lubricant inlet velocity

The first set of fluidic simulations on the lubrication system investigates the influence of lubricant velocity at the tool inlet. This velocity is controlled by the pumping system of the milling machine and varies between 77.6 and 126.7 m/s, corresponding to the operational conditions. In the simulations, the tool is assumed to be stationary. The lubricant velocity and pressure are calculated at the outlet of each channel (top channels and lateral channels) for six different inlet velocities. Both the original and modified components are modeled, and the results are presented in Table 1 and Fig. 12. In both design versions, the average lubricant pressure at the outlet increases as the inlet velocity increases. However, in the original design, the average pressure in the top channels (ranging from 12.72 to 33.38 MPa) is approximately 2.4 times higher than that in the lateral channels (ranging from 5.28 to 14.93 MPa) for all inlet velocities. This indicates a significant difference in fluidic resistance between the top and lateral channels, resulting in an unbalanced lubricant flow across the tool surfaces. In the redesigned version, lubricant flow balance is achieved. The average pressure in the top channels (ranging from 3.61 to 9.56 MPa) is only 1.2 times higher than that in the lateral channels (ranging from 3.05 to 8.09 MPa). This improvement is obtained by increasing the number of top channels from four to eight, which significantly reduces the output pressure in the top channels at the maximum inlet velocity (from 33.38 to 9.56 MPa, a reduction of 71.4%).

Similar effects are observed in the output lubricant velocity. In the original component, the velocities in the top channels (ranging from 159.56 to 259.27 m/s) are approximately 1.5 times higher than those in the lateral channels (ranging from 103.70 to 174.23 m/s). In contrast, in the redesigned version, the outlet velocity in the top channels (ranging from 84.73 to 138.56 m/s) is only 1.1 times higher than that in the lateral channels (ranging from 77.63 to 127.78 m/s).

In conclusion, the modified geometry of the channels enhances the uniformity of lubricant output pressure and

Table 1 Simulation results of lubricant pressure and velocity at channel outputs under variable inlet velocities and zero head angular velocity for both the original and redesigned components

				Lubricant inlet velocity (m/s)					
				77.6	89.6	100.1	109.7	118.5	126.7
Original design	Output pressure (MPa)	Top channels	average	12.72	16.88	20.96	25.18	29.51	33.38
			variance	0.06	0.07	0.07	0.09	0.11	0.11
			std. dev	0.23	0.26	0.27	0.29	0.33	0.34
		Lateral channels	average	5.28	7.31	9.30	11.36	13.41	14.93
			variance	0.01	0.02	0.08	0.05	0.04	0.19
			std. dev	0.10	0.14	0.29	0.21	0.19	0.44
	Output velocity (m/s)	Top channels	average	159.56	184.00	205.20	225.01	243.67	259.27
			variance	1.99	1.73	1.45	1.36	1.44	1.23
			std. dev	1.41	1.31	1.20	1.16	1.20	1.11
		Lateral channels	average	103.70	122.19	137.51	152.33	165.07	174.23
			variance	0.81	0.81	3.15	1.35	0.93	5.58
			std. dev	0.90	0.90	1.77	1.16	0.96	2.36
Modified design	Output pressure (MPa)	Top channels	average	3.61	4.79	6.09	7.27	8.61	9.56
			variance	0.06	0.04	0.07	0.08	0.31	0.33
			std. dev	0.24	0.20	0.27	0.28	0.56	0.57
		Lateral channels	average	3.05	4.08	5.10	6.20	7.01	8.09
			variance	0.04	0.01	0.02	0.02	0.05	0.08
			std. dev	0.21	0.08	0.12	0.15	0.22	0.28
	Output velocity (m/s)	Top channels	average	84.73	97.86	110.45	120.67	131.45	138.56
			variance	6.76	3.26	5.07	4.88	16.63	15.34
			std. dev	2.60	1.81	2.25	2.21	4.08	3.92
		Lateral channels	average	77.63	89.86	100.84	111.51	118.83	127.78
			variance	8.95	0.86	1.82	2.31	2.88	3.30
			std. dev	2.99	0.93	1.35	1.52	1.70	1.82

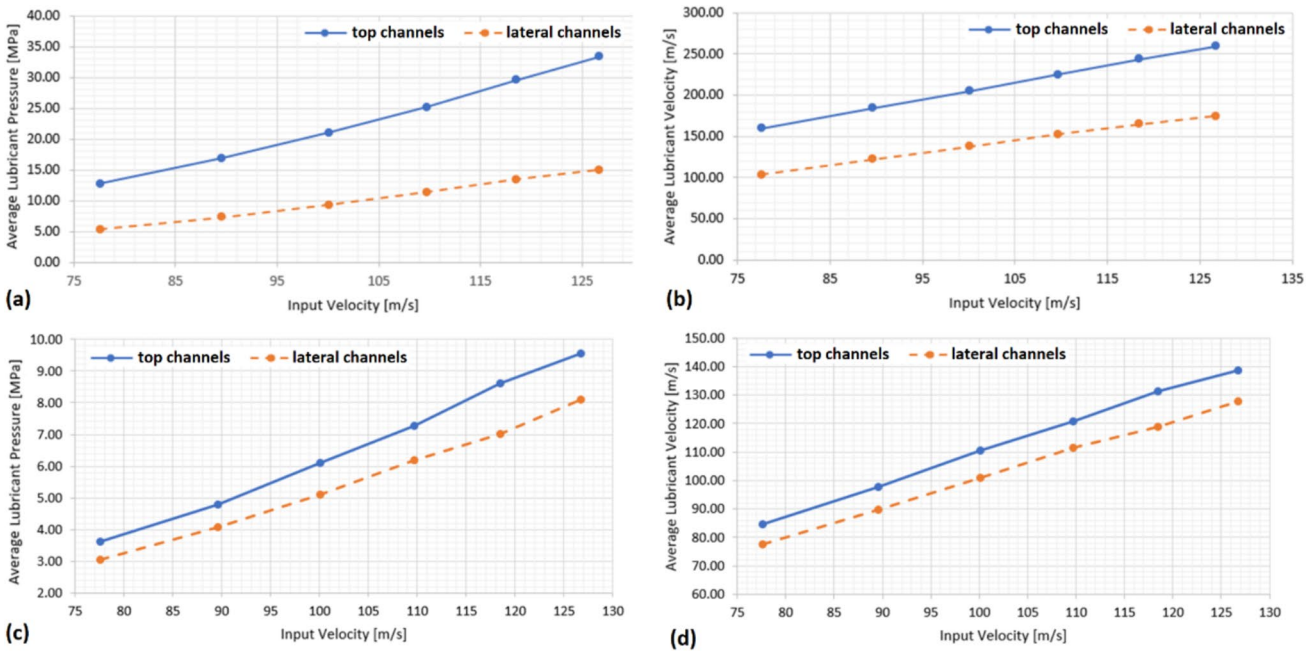

Fig. 12 Effect of lubricant inlet velocity (at zero rotation speed) on the output pressure and velocity averaged over the top and lateral channels in the original (**a**, **b**) and modified (**c**, **d**) components

velocity across the sixteen channels. Furthermore, considering the quality of spraying, Figs. 13 and 14 illustrate the distribution of lubricant pressure and velocity within the channels and around the cutting head. In the original component, the spray produced by the lateral channels is primarily directed radially outward and marginally reaches the cutting tips. With the modified design, the new shape of the lateral channels significantly improves the directionality and, consequently, the efficiency of lubrication. The figures necessarily present different axes to allow the visualization of pressure and velocity distribution. For a more straightforward quantitative comparison between the graphs, consider the ratios of the maximum pressures of the original and redesigned components, which are 2.78 (top channels), 2.00 (lateral channels), and 1.32 (cross section). Additionally, consider the ratios of the maximum velocities of the

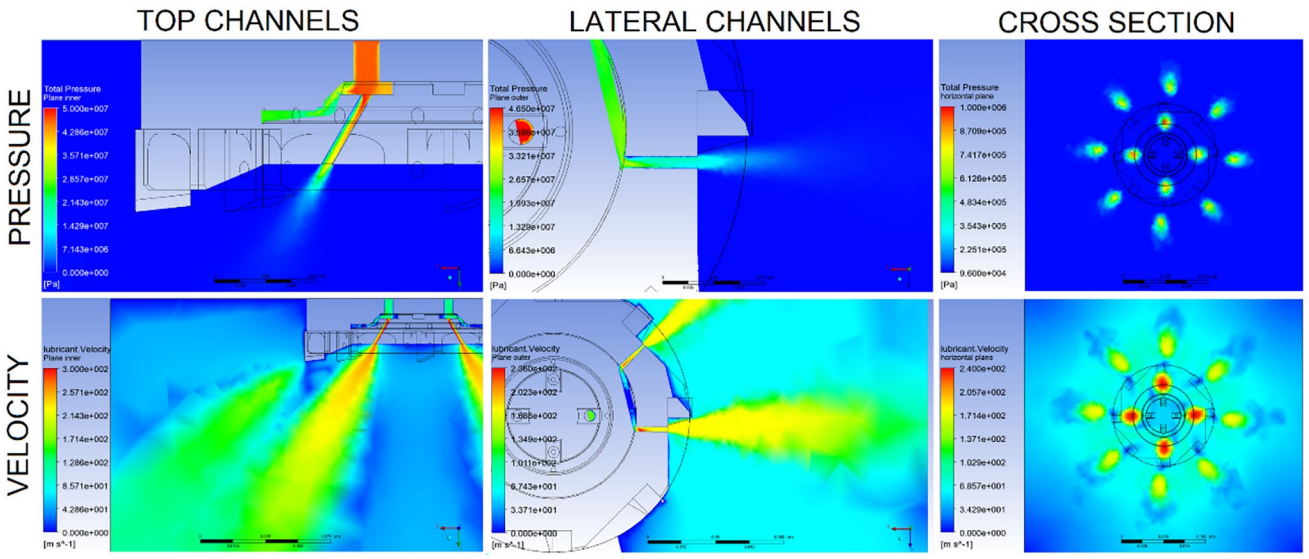

Fig. 13 Lubricant pressure and velocity distributions in the original component, calculated using CFD simulations with an inlet velocity of 126.7 m/s and zero rotation speed

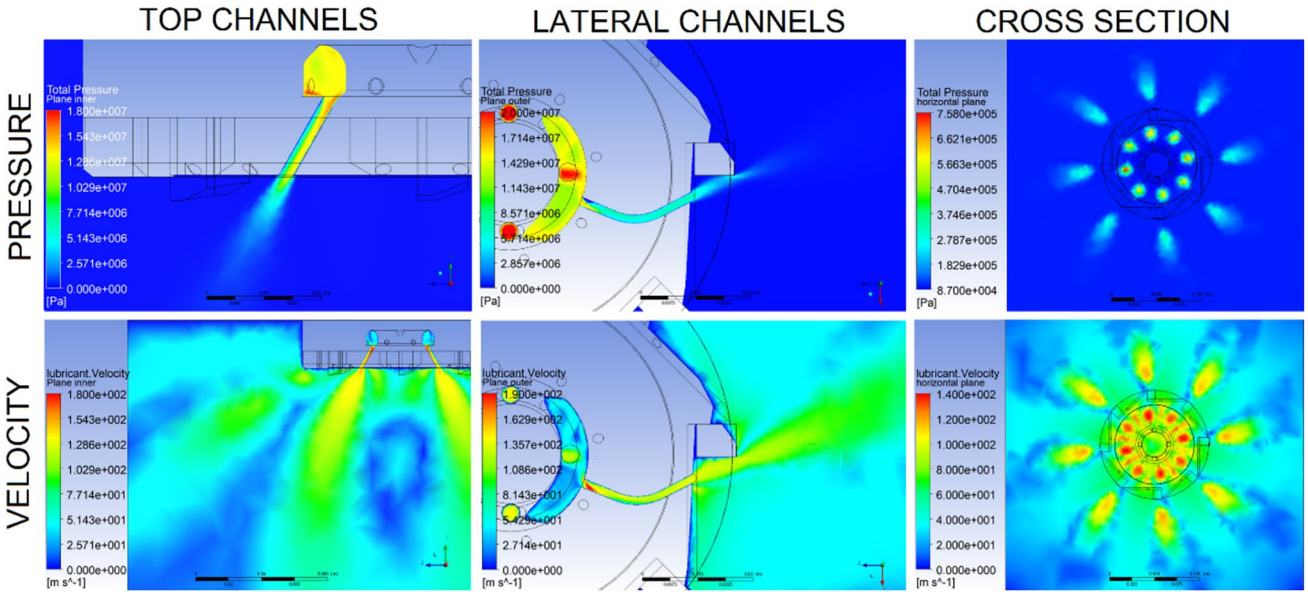

Fig. 14 Lubricant pressure and velocity distributions in the redesigned component, calculated using CFD simulations with an inlet velocity of 126.7 m/s and zero rotation speed

original and redesigned components, which are 1.67 (top channels), 1.24 (lateral channels), and 1.71 (cross section).

6.2.2 Effect of rotation velocity

In this case, the simulations investigate the effects of rotational velocity on lubrication. Six values of rotational speed are imposed within the range of 0 to 1047 rad/s, while the lubricant velocity and pressure are calculated at the output of each channel. The lubricant velocity at the tool inlet is maintained at 100 m/s. The results are presented in Table 2 and Fig. 15.

The lubricant pressure at the output decreases as the rotational speed increases. This phenomenon is attributed to the centrifugal acceleration, which is proportional to the rotational velocity and acts on the fluid mass, facilitating flow through the channels. This effect is more pronounced in the lateral channels, which are oriented along the radial direction of the cutting head. In the original component, the pressure reduction in the top channels (from 21.08 to 20.34 MPa) and lateral channels (from 9.07 to 7.80 MPa) corresponds to reductions of 3.5% and 14.0%, respectively, when subjected to angular velocities ranging from 0 to 1047 rad/s. In the redesigned component, under the same conditions, the fluid pressure reduction in the top channels (from 5.84 to 5.13 MPa) and lateral channels (from 4.99 to 3.87 MPa) is 12.1% and 22.4%, respectively. Thus, the new channel shape and configuration enhance fluid flow by leveraging the rotational velocity of the tool.

In the original component, the average lubricant velocity at the channel outputs remains nearly constant with increasing angular velocity. At zero rotational velocity, the fluid velocity is measured at 205.83 m/s and 136.04 m/s at the top and lateral channel outputs, respectively. The variations at 1047 rad/s are − 1.02% and + 0.65%, respectively. This result is consistent with the previously described nearly constant output pressure observed in the original component as rotational velocity increases. The situation in the redesigned component differs slightly: the fluid velocity in the lateral channels increases from 100.25 m/s to 102.26 m/s (a rise of 2.0%), while it decreases in the top channels from 107.92 m/s to 105.08 m/s (a decline of 2.6%). The enhanced fluid flow, facilitated by the parabolic shape of the lateral channels, leads to a higher output velocity. Conversely, the reduction in velocity in the top channels can be attributed to the presence of the internal reservoir, which acts as a connection to the lateral channels. This shared source results in the observed flow balance between the top and lateral channel paths.

Figures 16 and 17 illustrate the lubricant pressure and velocity distributions within the channels and around the cutting head for both versions. The redesign significantly enhances fluid uniformity around the component, and the lateral spray is effectively directed toward the cutting tips due to the deviation induced by rotation. The figures necessarily present different axes to allow the visualization of pressure and velocity distribution. For a more straightforward quantitative comparison between the graphs, consider the ratios of the maximum pressures of the original and redesigned components, which are 2.68 (top channels), 2.46 (lateral channels), and 1.73 (cross section). Additionally, consider the ratios of the maximum velocities of the

Table 2 Simulation results of lubricant pressure and velocity at channel outputs under variable head angular velocities and an inlet lubricant velocity of 100 m/s for the original and redesigned components

				Cutting head angular velocity (rad/s)					
				0	200	400	600	800	1047
Original design	Output pressure (MPa)	Top channels	average	21.08	20.97	20.84	20.73	20.68	20.34
			variance	0.09	0.09	0.08	0.08	0.09	0.08
			std. dev	0.29	0.30	0.28	0.28	0.30	0.29
		Lateral channels	average	9.07	9.08	8.94	8.75	8.45	7.80
			variance	0.05	0.02	0.04	0.05	0.03	0.03
			std. dev	0.23	0.14	0.20	0.23	0.16	0.17
	Output velocity (m/s)	Top channels	average	205.83	205.38	204.85	204.60	204.74	203.73
			variance	1.75	1.77	1.49	1.49	1.73	1.65
			std. dev	1.32	1.33	1.22	1.22	1.32	1.29
		Lateral channels	average	136.04	136.30	136.34	137.18	137.64	136.92
			variance	1.99	0.93	1.29	2.21	1.17	1.30
			std. dev	1.41	0.96	1.14	1.49	1.08	1.14
Modified design	Output pressure (MPa)	Top channels	average	5.84	5.83	5.86	5.66	5.44	5.13
			variance	0.34	0.39	0.32	0.28	0.17	0.20
			std. dev	0.58	0.63	0.57	0.53	0.42	0.44
		Lateral channels	average	4.99	4.95	4.80	4.67	4.36	3.87
			variance	0.08	0.03	0.02	0.04	0.05	0.05
			std. dev	0.28	0.19	0.15	0.21	0.22	0.22
	Output velocity (m/s)	Top channels	average	107.92	107.97	108.68	107.46	106.52	105.08
			variance	26.57	30.47	24.16	22.05	13.14	14.20
			std. dev	5.15	5.52	4.92	4.70	3.62	3.77
		Lateral channels	average	100.25	100.20	100.11	101.18	101.53	102.26
			variance	4.64	2.13	2.90	4.85	4.79	3.90
			std. dev	2.15	1.46	1.70	2.20	2.19	1.98

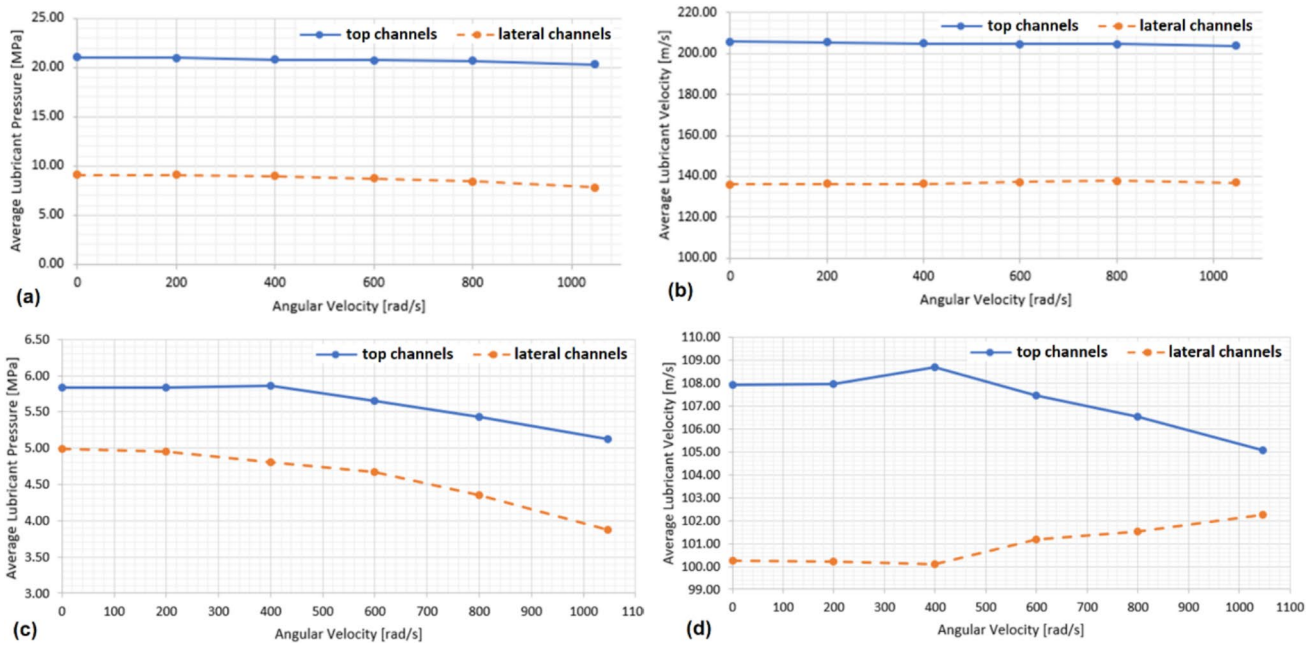

Fig. 15 Effect of tool angular velocity (at a lubricant inlet velocity of 100 m/s) on the averaged lubricant pressure and velocity at the outlets of the top and lateral channels in the original (**a**, **b**) and modified (**c**, **d**) components

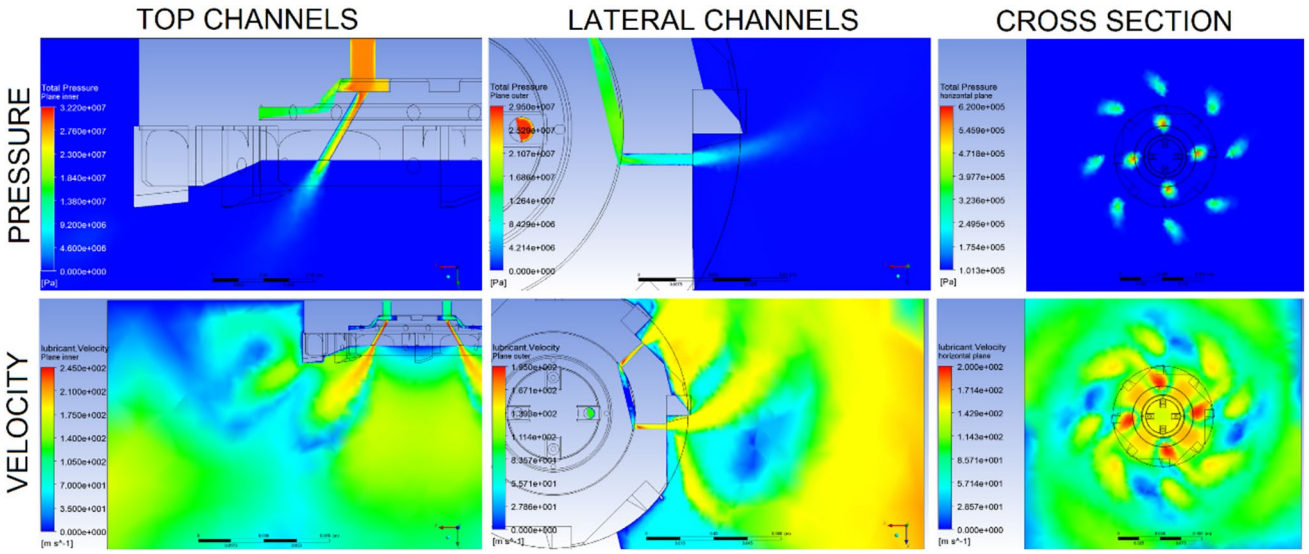

Fig. 16 Lubricant pressure and velocity distributions in the original component, calculated using CFD simulations with a cutting head angular velocity of 1047 rad/s and a lubricant inlet velocity of 100 m/s

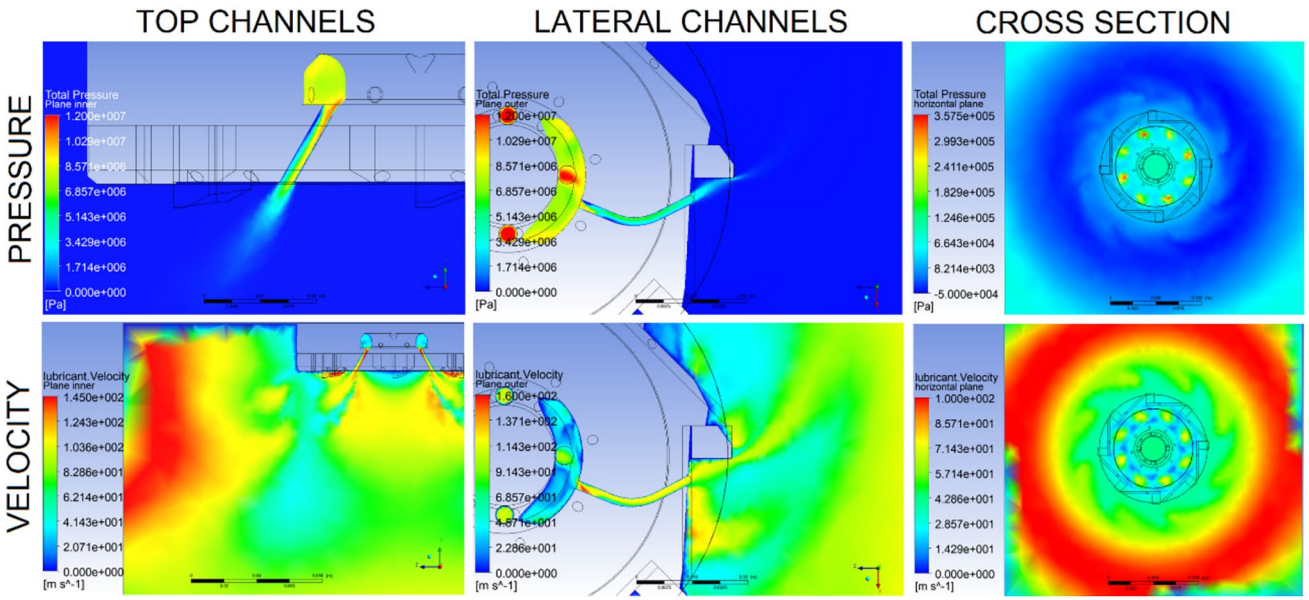

Fig. 17 Lubricant pressure and velocity distributions in the redesigned component, calculated using CFD simulations with a cutting head angular velocity of 1047 rad/s and a lubricant inlet velocity of 100 m/s

original and redesigned components, which are 1.69 (top channels), 1.22 (lateral channels), and 2.00 (cross section).

6.3 Experimental results

The torsional stiffness of both the original and redesigned cutting head tools is measured using the experimental setup described previously. The strain gauges affixed to the surface of the components in a half-bridge configuration yield the strain values presented in Fig. 18. The maximum strain value measured on the redesigned head is 77.41 μm/m, which represents an increase of 84% compared to the original component, which measured 42.06 μm/m. This increment in strain is attributed to the reduction in mass of the component, which consequently leads to a decrease in torsional stiffness.

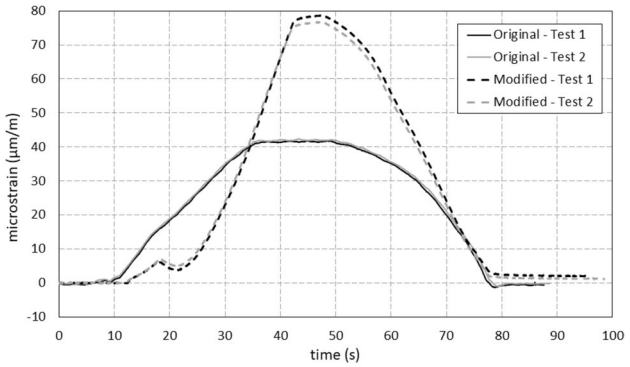

Fig. 18 Experimental results of the strain measured on the component surface subjected to torque varying from 0 to 685 Nm. The strain values for the original component (represented by solid lines) and the redesigned component (represented by dashed lines) are presented

Table 3 Comparison of experimental results and numerical simulations of the strain values on the surface of both the original and redesigned components under a torsional torque of 685 Nm

	Original component (μm/m)		Modified component (μm/m)	
	Test 1	Test 2	Test 1	Test 2
Experiments	41.63	42.50	78.51	76.31
FEM simulation	39.90		78.77	
Deviation	4.15%	6.11%	− 0.33%	− 3.22%

6.4 Discussions

Table 3 presents a comparison between the strain values measured experimentally and those calculated through finite element method (FEM) simulations at maximum torque. The results exhibit good agreement, with a maximum error of 6.11% for the original component and 3.22% for the redesigned component. This comparison validates that the proposed modeling strategy is effective in accurately predicting the structural behavior of the cutting head. Table 4 summarizes the properties of both the original and redesigned components for AM production. Specifically, the following results were achieved:

(a) The mass of the redesigned component is reduced by 33.9%, decreasing from 1941.3 g for the original design to 1282.3 g.
(b) The maximum stress induced by rotation is decreased by 11.4% in the redesigned component; however, the stress resulting from the cutting torque increases by 79.3% due to the weight reduction process. Given the greater influence of the former effect, the overall maximum stress in the redesigned version is reduced by 12.2%.
(c) The final component exhibits higher values of maximum overall displacement under load (+37.9%). However, these displacements occur away from the functional regions (such as insert supports and cutting tips), ultimately enhancing the operational accuracy of the component.
d) The newly designed parabolic shape of the lateral lubrication channels provides improved orientation of the spray on the cutting tips, resulting in increased lubrication and cooling efficiency.
(e) The revised configuration of the lubrication system enhances output pressure uniformity among channels and reduces performance variations under varying

Table 4 Comparison of the global properties between the original cutting head tool and the redesigned version for AM production

		Original component	Modified component	Variation (%)
Volume (mm^3)	V	438,413	289,598	− 33.9
	V_{body}	404,941 (body)		
	V_{cover}	33,472 (cover)		
Mass (g)	m	1941.3	1282.3	− 33.9
	m_{body}	1793.1 (body)		
	m_{cover}	148.2 (cover)		
Moments of inertia at center of mass ($g{\cdot}mm^2$)	I_{xx}	$21.04{\cdot}10^5$	$3.62{\cdot}10^5$	− 82.8
	I_{yy}	$20.49{\cdot}10^5$	$3.67{\cdot}10^5$	− 82.1
	I_{zz}	$33.66{\cdot}10^5$	$5.61{\cdot}10^5$	− 83.3
Equivalent stress (Mpa)	$\sigma_{rotation}$	969	858	− 11.4
	σ_{torque}	184	330	+79.3
	$\sigma_{overall}$	974	855	− 12.2
Equivalent displacement (mm)	$D_{rotation}$	$1.92{\cdot}10^{-1}$	$2.76{\cdot}10^{-1}$	+43.7
	D_{torque}	$2.61{\cdot}10^{-2}$	$3.51{\cdot}10^{-2}$	+34.5
	$D_{overall}$	$2.06{\cdot}10^{-1}$	$2.84{\cdot}10^{-1}$	+37.9
Torsional stiffness (Nm/deg)	k_{tor}	37,118	27,974	− 24.6

pumping system regimes. Simultaneously, the beneficial effect of centrifugal acceleration on lubricant flow is amplified, improving the cleaning of the workpiece from debris.

(f) The features introduced in the redesigned cutting head are developed in accordance with the design for additive manufacturing (DfAM) approach, rendering the component suitable for production using powder micromelting processes.

The modification of the shape of the eight lateral channels from straight to curved improves lubricant directionality, cooling performance, and fluid extraction through rotational centrifugal force. CFD analysis also confirms the enhanced fluidic performance of the top channels, where the individual inlet and outlet pressure and velocity values are superior compared to the original design. In the modified component, the shape of the top channels remains straight, but their number has increased from four to eight. While this change does not affect the local fluid pressure and velocity values, it effectively doubles the fluid flow, resulting in greater efficiency in metal chip removal operations.

7 Conclusions

The design, simulation, and experimental characterization methods applied to the cutting head tool for milling machines are tailored for production via AM. The implementation of DfAM criteria, in conjunction with traditional mechanical design principles, is essential to accommodate the requirements imposed by the AM process. Additionally, within the same redesign solution, component lightweighting is combined with the consolidation of multiple parts and enhancements in functionality. The reduction in mass is linked to improved handling, lower energy consumption during operations, and decreased production costs. Furthermore, the structural properties are modified to provide enhanced stress and strain distributions concerning maximum values and accuracy, thereby increasing the expected component lifespan and functionality. The revised lubrication system ensures uniform, consistent, and well-oriented lubricant spraying, leading to improved cooling capabilities and efficiency in debris removal. In conclusion, the integration of multiple design objectives, while complicated by the interdependencies involved, has been successfully achieved through the amalgamation of structural and fluidic simulations with functional design considerations and process constraints.

Appendix

Mesh sensitivity analysis

To ensure the reliability of the results, a mesh sensitivity analysis was conducted as part of the structural analysis. To reduce computational costs, the study initially focused on a one-eighth segment of the component. Once an optimal mesh configuration was determined, the same mesh settings were applied to the entire model in this work. Table 5 summarizes the various mesh configurations along with the corresponding maximum von Mises stress and displacement values, which served as the primary quantities of interest. Figure 19 illustrates the mesh resolution, while Figs. 20 and 21 present the mesh convergence trends.

Table 5 Different number of nodes setting and the resulting maximum stress and displacement

Number of nodes	Max von Mises stress [MPa]	Max displacement [mm]
4283	45.97	0.00960
10,102	40.73	0.00991
26,384	39.82	0.01012
77,273	40.82	0.01019
174,689	40.63	0.01023
296,528	40.84	0.01024

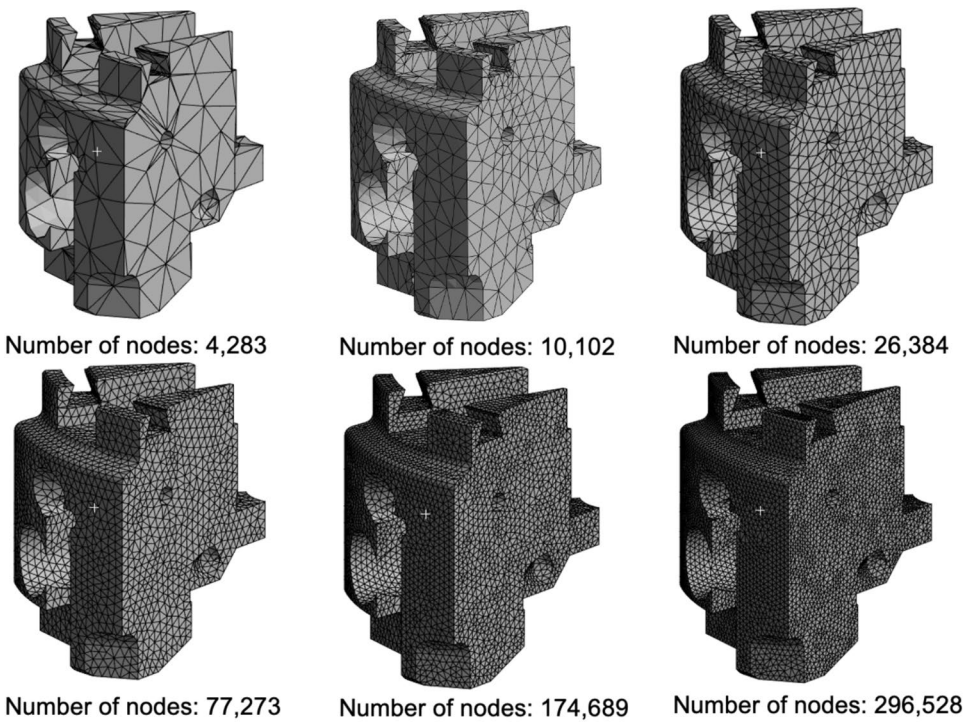

Fig. 19 Different mesh sizes with corresponding total number of nodes

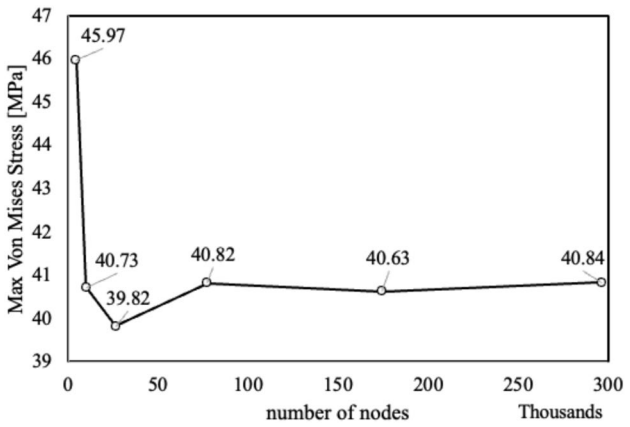

Fig. 20 The convergence of maximum von Mises stresses with different mesh settings

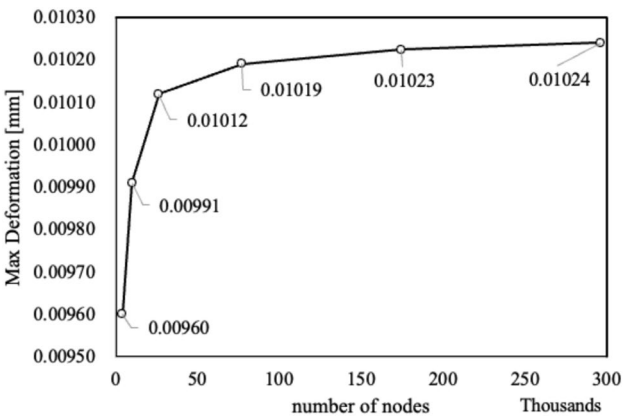

Fig. 21 The convergence of maximum deformation with different mesh settings

Funding Open access funding provided by Politecnico di Torino within the CRUI-CARE Agreement.

Data availability Data are available upon request to the authors.

Declarations

Conflict of interest The authors declare that they do not have any competing interests/ onflict of interest in relation to this work.

Open Access This article is licensed under a Creative Commons Attribution 4.0 International License, which permits use, sharing, adaptation, distribution and reproduction in any medium or format, as long as you give appropriate credit to the original author(s) and the source, provide a link to the Creative Commons licence, and indicate if changes were made. The images or other third party material in this article are included in the article's Creative Commons licence, unless indicated otherwise in a credit line to the material. If material is not included in the article's Creative Commons licence and your intended use is not permitted by statutory regulation or exceeds the permitted use, you will need to obtain permission directly from the copyright holder. To view a copy of this licence, visit http://creativecommons.org/licenses/by/4.0/.

References

1. Attaran M (2017) The rise of 3-D printing: the advantages of additive manufacturing over traditional manufacturing. Bus Horiz. https://doi.org/10.1016/j.bushor.2017.05.011
2. Schniederjans DG (2017) Adoption of 3D-printing technologies in manufacturing: a survey analysis. Int J Prod Econ. https://doi.org/10.1016/j.ijpe.2016.11.008
3. Savolainen J, Collan M (2020) How additive manufacturing technology changes business models? – Review of literature. Addit Manuf. https://doi.org/10.1016/j.addma.2020.101070
4. Brecher C, Utsch P, Klar R, Wenzel C (2010) Compact design for high precision machine tools. Int J Mach Tools Manuf. https://doi.org/10.1016/j.ijmachtools.2009.11.007
5. Wang ZG, Cheng X, Nakamoto K, Kobayashi S, Yamazaki K (2010) Design and development of a precision machine tool using counter motion mechanisms. Int J Mach Tools Manuf. https://doi.org/10.1016/j.ijmachtools.2009.10.014
6. Hanzl P, Zetková I (2019) Benefits of a new approach to designing milling cutter using metal additive manufacturing. Manuf Technol. https://doi.org/10.21062/ujep/301.2019/a/1213-2489/mt/19/3/385
7. Hanzl P, Zetková I, Zetek M (2020) Comparison of lightweight and solid milling cutter capabilities. Manuf Technol. https://doi.org/10.21062/mft.2020.008
8. Yang S, Page T, Zhang Y, Zhao YF (2020) Towards an automated decision support system for the identification of additive manufacturing part candidates. J Intell Manuf. https://doi.org/10.1007/s10845-020-01545-6
9. Adam GAO, Zimmer D (2014) Design for additive manufacturing-element transitions and aggregated structures. CIRP J Manuf Sci Technol. https://doi.org/10.1016/j.cirpj.2013.10.001
10. Hällgren S, Pejryd L, Ekengren J (2016) (Re)Design for additive manufacturing. Procedia CIRP. https://doi.org/10.1016/j.procir.2016.04.150
11. Hanzl P, Zetková I, Zetek M (2019) Specially designed lattice structure for milling cutter supported by FEA. Manuf Technol. https://doi.org/10.21062/ujep/337.2019/a/1213-2489/MT/19/4/579
12. Bertolino G, Montemurro M, De Pasquale G (2019) Multi-scale shape optimisation of lattice structures: an evolutionary-based approach. Int J Interact Des Manuf. https://doi.org/10.1007/s12008-019-00580-9
13. Großmann A, Weis P, Clemen C, Mittelstedt C (2020) Optimization and re-design of a metallic riveting tool for additive manufacturing—a case study. Addit Manuf. https://doi.org/10.1016/j.addma.2019.100892
14. Montalto A, Graziosi S, Bordegoni M, Di Landro L, van Tooren MJL (2020) An approach to design reconfigurable manufacturing tools to manage product variability: the mass customisation of eyewear. J Intell Manuf. https://doi.org/10.1007/s10845-018-1436-5
15. Klahn C, Leutenecker B, Meboldt M (2014) Design for additive manufacturing - supporting the substitution of components in series products. Procedia CIRP. https://doi.org/10.1016/j.procir.2014.03.145
16. Bikas H, Stavropoulos P, Chryssolouris G (2016) Additive manufacturing methods and modeling approaches: a critical review. Int J Adv Manuf Technol. https://doi.org/10.1007/s00170-015-7576-2
17. Sandwik 2020 "Design the unseen - optimize performance, Sandwik," https://www.additive.sandvik/en/theadditive-advantage/design-the-unseen-optimize-performance/, 24 Nov 2020
18. Hanzl P, Zetek M, Rulc V, Purš H, Zetková I (2019) Finite element analysis of a lightweight milling cutter for metal additive manufacturing. Manuf Technol. https://doi.org/10.21062/ujep/367.2019/a/1213-2489/MT/19/5/753
19. Bakošová D (2018) Dynamic mechanical analysis of rubber mixtures filled by carbon nanotubes. Manuf Technol. https://doi.org/10.21062/ujep/103.2018/a/1213-2489/MT/18/3/345
20. De Pasquale G, Sibona S (2021) Hybrid materials based on polymers-filled AM steel lattices with energy absorption capabilities. Mech Adv Mater Struct. https://doi.org/10.1080/15376494.2020.1871536
21. De Pasquale G, Luceri F, Riccio M (2019) Experimental characterization of SLM and EBM cubic lattice structures for lightweight applications. Exp Mech. https://doi.org/10.1007/s11340-019-00481-8
22. De Pasquale G, Tagliaferri A (2019) Modeling and characterization of mechanical and energetic elastoplastic behavior of lattice structures for aircrafts anti-icing systems. Proc Inst Mech Eng Part C J Mech Eng Sci. https://doi.org/10.1177/0954406219853857
23. Wang R, Shang J, Li X, Luo Z, Wu W (2018) Vibration and damping characteristics of 3D printed Kagome lattice with viscoelastic material filling. Sci Rep. https://doi.org/10.1038/s41598-018-27963-4
24. Miyaguchi T, Masuda M, Takeoka E, Iwabe H (2001) Effect of tool stiffness upon tool wear in high spindle speed milling using small ball end mill. Precis Eng. https://doi.org/10.1016/S0141-6359(01)00067-8
25. Coluccia A, De Pasquale G (2023) Strain-based method for fatigue failure prediction of additively manufactured lattice structures. Nature Sci Rep 13:22775. https://doi.org/10.1038/s41598-023-49846-z
26. De Pasquale G, Coluccia A (2023) Modeling and experimental validation of CFRP-metal joints utilizing 3D additively manufactured anchors. J Manuf Sci Eng 145(11):111004. https://doi.org/10.1115/1.4063110
27. De Pasquale G, Altunok FE, Ursi F (2023) Investigation of the mechanical strength of CFRP with co-cured additively manufactured metal inserts. Proc Struct Int 47:573–578. https://doi.org/10.1016/j.prostr.2023.07.067
28. Coluccia A, Jiang G, Meyer G, De Pasquale G, Mittelstedt C (2022) Nonlinear static and dynamic modeling of energy absorption lattice structures behavior. Mech Adv Mat Struct. https://doi.org/10.1080/15376494.2022.2064016

29. De Pasquale G, Coluccia A (2022) Fatigue failure prediction in lattice structures through numerical method based on de-homogenization process. Proc Struct Int 41:535–543. https://doi.org/10.1016/j.prostr.2022.05.06
30. De Pasquale G, Altunok FE (2025) Multiphase modeling of matrix/fiber-related damaging mechanism in multimaterial additively manufactured joints with 3D interlocking. Eng Fail Anal 170:109272. https://doi.org/10.1016/j.engfailanal.2025.109272
31. Zhang C, Wang S, Li J, Zhu Y, Peng T, Yang H (2020) Additive manufacturing of products with functional fluid channels: a review. Addit Manuf. https://doi.org/10.1016/j.addma.2020.101490
32. Ilčík J, Koutný D, Paloušek D (2014) Geometrical accuracy of the metal parts produced by selective laser melting: Initial tests. Lecture Notes Mech Eng. https://doi.org/10.1007/978-3-319-05203-8_76
33. Poprawe R, Hinke C, Meiners W, Schrage J, Bremen S, Merkt S (2015) SLM production systems: recent developments in process development, machine concepts and component design. In: Brecher C (ed) Advances in Production Technology. Lecture Notes in Production Engineering. Springer, Cham. https://doi.org/10.1007/978-3-319-12304-2_5
34. De Pasquale G, Luceri F, Riccio M (2019) Experimental evaluation of selective laser melting process for optimized lattice structures. Proc Inst Mech Eng Part E J Process Mech Eng. https://doi.org/10.1177/0954408918803194
35. Emmelmann C, Sander P, Kranz J, Wycisk E (2011) Laser additive manufacturing and bionics: redefining lightweight design. Phys Procedia. https://doi.org/10.1016/j.phpro.2011.03.046
36. Sandwik (2020) "How to reduce vibration in metal cutting," https://www.sandvik.coromant.com/sitecollectiondocuments/downloads/global/technical%20guides/en-gb/c-2920-23.pdf, 24 Nov 2020
37. Alamos FJ, Schiltz J, Kozlovsky K, Attardo R, Tomonto C, Pelletiers T, Schmid SR (2020) Effect of powder reuse on mechanical properties of Ti-6Al-4V produced through selective laser melting. Int J Refract Met Hard Mater 91:105273. https://doi.org/10.1016/j.ijrmhm.2020.105273
38. Wohlers Report 2024: Additive manufacturing and 3D printing state of the industry. ASTM International. Wohlers Associates, 2024. Available at: https://wohlersassociates.com/product/wr2024/. Accessed Mar 2025
39. Moresco (2020) "Cutting Fluids," http://www.moresco.co.th/products/cutting-fluids/. Accessed Mar 2025
40. Gokhale NS, Deshpande SS, Bedekar SV, Thite AN (2008) Practical finite element analysis. Finite to Infinite Editor, Maharashtra. ISBN: 978-81-906195-0-9
41. Edwards P, Ramulu M (2014) Fatigue performance evaluation of selective laser melted Ti-6Al-4V. Mater Sci Eng A. https://doi.org/10.1016/j.msea.2014.01.041
42. Keil S (2017) Technology and practical use of strain gages with particular consideration of stress analysis using strain gages. Wilhelm Ernst & Sohn Editor. https://doi.org/10.1002/9783433606667

Publisher's Note Springer Nature remains neutral with regard to jurisdictional claims in published maps and institutional affiliations.